

PCCP

Accepted Manuscript



This is an *Accepted Manuscript*, which has been through the Royal Society of Chemistry peer review process and has been accepted for publication.

Accepted Manuscripts are published online shortly after acceptance, before technical editing, formatting and proof reading. Using this free service, authors can make their results available to the community, in citable form, before we publish the edited article. We will replace this *Accepted Manuscript* with the edited and formatted *Advance Article* as soon as it is available.

You can find more information about *Accepted Manuscripts* in the [Information for Authors](#).

Please note that technical editing may introduce minor changes to the text and/or graphics, which may alter content. The journal's standard [Terms & Conditions](#) and the [Ethical guidelines](#) still apply. In no event shall the Royal Society of Chemistry be held responsible for any errors or omissions in this *Accepted Manuscript* or any consequences arising from the use of any information it contains.

Xenon NMR of liquid crystals confined to cylindrical nanocavities: A simulation study[†]

Jouni Karjalainen,^a Juha Vaara,^a Michal Straka^b and Perttu Lantto^a

Received Xth XXXXXXXXXXXX 20XX, Accepted Xth XXXXXXXXXXXX 20XX

First published on the web Xth XXXXXXXXXXXX 200X

DOI: 10.1039/b000000x

Applications of liquid crystals (LCs), such as smart windows and the ubiquitous display devices, are based on controlling the orientational and translational order in a small volume of LC medium. Hence, understanding the effects of confinement to the liquid crystal phase behaviour is essential. The NMR shielding of ¹²⁹Xe atoms dissolved in LCs constitutes a very sensitive probe to the details of LC environment. Linking the experimental results to microscopic phenomena calls for molecular simulations. In this work, the NMR shielding of atomic ¹²⁹Xe dissolved in a uniaxial thermotropic LC confined to nanosized cylindrical cavities is computed from coarse-grained (CG) isobaric Monte Carlo (MC) simulations with a quantum-chemically (QC) pre-parameterised pairwise-additive model for the Xe nuclear shielding tensor. We report the results for the ¹²⁹Xe nuclear shielding and its connection to the structure and order of the LC appropriate to two different cavity sizes, as well as a comparison to the results of bulk (non-confined) simulations. We find that the confinement changes the LC phase structure dramatically and gives rise to the coexistence of varying degrees of LC order, which is reflected in the Xe shielding. Furthermore, we qualitatively reproduce the behaviour of the mean ¹²⁹Xe chemical shift with respect to temperature for atomic Xe dissolved in LC confined to controlled-pore glass materials. In the small-radius cavity the nematic – paranematic phase transition is revealed only by the anisotropic component of the ¹²⁹Xe nuclear shielding. In the larger cavity, the nematic – paranematic – isotropic transition is clearly seen in the Xe shielding. The simulated ¹²⁹Xe NMR shielding is insensitive to the smectic-A – nematic transition, since in the smectic-A phase, the Xe atoms largely occupy the imperfect layer structure near the cavity walls. The direct contribution of the cavity wall to ¹²⁹Xe nuclear shielding is dependent on the cavity size but independent of temperature. Our results show that the combination of CG simulations and a QC pre-parameterised ¹²⁹Xe NMR shielding allows efficient studies of the phase behaviour and structure of complex systems containing thousands of molecules, and brings us closer to the simulation of NMR experiments.

1 Introduction

Liquid crystals (LCs) display complex phase behaviour when confined to small cavities of porous materials.¹ The confinement can shift transition temperatures and either enhance or suppress the ordering of the molecules, depending on the size and the shape of the confining space, the properties of the confining surfaces, and the liquid crystal molecules themselves.

The most common LC phases include the orientationally or-

dered nematic and the translationally ordered smectic phases.² In the uniaxial nematic phase (N) the long axes of the LC molecules are on average aligned along a common direction, which is called the director. The smectic-A phase (SmA) possesses orientational order similarly to the uniaxial nematic phase and, additionally, the molecules are positionally ordered in layers perpendicular to the director. In a thermotropic LC, typically a sequence of increasingly (decreasingly) ordered phases is observed as the material is slowly cooled (heated). When an external field induces nematic order to an isotropic LC, the resulting phase is called paranematic (PN).

Previously we have shown³ that in long, smooth-walled cylindrical pores, small in diameter, the confinement can sustain substantial orientational order far above the bulk nematic - isotropic (N-I) transition temperature, resulting in a partially oriented PN phase. The findings are backed up by recent experimental work on cylindrically confined LCs.⁴⁻⁷ The appearance of smectic layering was found to be nearly unaffected by the confinement, although the translational order was slightly lower near the wall.

[†] Electronic Supplementary Information (ESI) available: Description of the parallel tempering procedure; review of the Gay-Berne liquid crystal model; review of the interaction between Lennard-Jones and Gay-Berne particles and justification for the potential parameterisation chosen in this paper; description of the calculation of order parameters; parameterisation of the Xe-wall interaction; description of the parameterisation of the ¹²⁹Xe nuclear shielding interactions; derivation of the Xe-wall shielding interaction; calculation of the radial profile of the translational order parameter. See DOI: 10.1039/b000000x/

^a NMR Research Group, University of Oulu, Oulu, Finland. Fax: +358-8-553-1287; Tel: +358-0294-48-1342; E-mail: jouni.karjalainen@oulu.fi

^b Institute of Organic Chemistry and Biochemistry, Academy of Sciences of the Czech Republic, Flemingovo n. 2., 16610 Prague, Czech Republic

Liquid crystals have been successfully studied with nuclear magnetic resonance (NMR).⁸ Xenon has many features that make it an excellent probe atom for NMR studies of various host materials.^{8–14} It is chemically inert and has a large electron cloud that is sensitive to its surroundings. The large natural abundance of the ^{129}Xe isotope, its relatively large magnetic dipole moment and the possibility of hyperpolarization increases the usefulness of ^{129}Xe NMR experiments.

The present work focuses on investigating the NMR chemical shift of ^{129}Xe dissolved in a uniaxial LC confined to a cylindrical cavity in a mesoporous material.^{10,11} We compute the orientational and translational order parameters from simulations and show how the changes in LC order, due to confinement in cavities with different radii, are reflected in the NMR parameters of the dissolved Xe atoms. For this purpose we use a quantum-chemically pre-parameterised, pairwise-additive model for the NMR interactions.^{15,16} We focus on the ^{129}Xe nuclear magnetic shielding computed from snapshots of constant-pressure parallel tempering (PT) simulations of a coarse-grained molecular model. The LCs are modeled with the Gay-Berne (4.4, 20, 1, 1) (GB) potential in long, smooth-walled cavities. The chosen particle-wall interaction favours homogeneous planar anchoring, the alignment of the long axes of the molecules along the wall.

We compare the simulated ^{129}Xe NMR shielding to previously measured NMR results for ^{129}Xe dissolved in LCs confined to the cavities of controlled pore glass (CPG) materials, CPG81 and CPG156.^{10,11} We find that the confinement changes the LC phase structure dramatically, which is reflected in the ^{129}Xe NMR shielding. In a small-radius cavity, the transition from the nematic to the paranematic phase is visible only in the anisotropic contribution to the Xe nuclear shielding. When the cavity size increases, the smooth nematic - paranematic - isotropic transition is reflected clearly also in the observable ^{129}Xe NMR shielding averaged over the entire sample, as well as seen in the local shielding as a function of the radial location of the xenon atom in different regions (near the wall or center) of the cavity. The smectic-*A* – nematic transition is practically unnoticeable in the nuclear shielding parameters of the ^{129}Xe atom in the confined systems, whereas it is seen as a change of slope in the Xe shielding curves of the bulk system. This is due to the major contribution to ^{129}Xe NMR shielding arising from the distorted layering of the smectic-*A* phase near the cavity wall. The direct contribution of the wall to ^{129}Xe nuclear shielding is practically temperature-independent but depends on the cavity size.

2 Simulations

The methodological workflow used here to calculate the NMR shielding of Xe nuclei from simulations is outlined in Fig. 1. We encourage the readers not interested in the technical de-

tails to review the figure and then jump to results in Sec. 5. Fig. 1 gives a map for locating the particular aspects of the simulation model.

We use our recently developed, coarse-grained model for a generic uniaxial LC and a smooth-walled cylindrical cavity.³ The model is reviewed in Secs. 3.1 and 3.3 below. The necessary extensions to the model, due to the presence of Xe solutes, are presented in Sec. 3.2 in the main text and in Sec. 5 of the Electronic Supplementary Information (ESI) of this Article,[†] in which we also justify the selection of the parameters for the interactions. We use pairwise additive interactions to construct the ^{129}Xe nuclear shielding, as presented in Sec. 4. The simulation parameters and our work in general are represented in reduced units, which are based on the Gay-Berne (GB) potential¹⁸ parameters, and are detailed in Sec. 3.1. The present simulations were performed for a bulk LC and for confined LCs in cavities with radii $R = 9$ (R9) and $R = 18$ (R18), at a fixed pressure $P = 2.0$. For each system, the temperature range $T = 0.9 \dots 2.0$ was covered with two parallel tempering (PT)¹⁹ simulation sequences. The PT algorithm is briefly reviewed in Sec. 1 of the ESI.[†]

The selected temperature range and pressure cover the crystal (Cr), SmA, N and isotropic (I) phases for bulk LC.^{3,15,20,21} For the R9 system the sharp N-I transition of bulk LC is converted to a continuous N-PN transition and the isotropic phase is not observed below $T = 2.0$.³ Here, the bulk system and the tight confinement of the R9 system present the two extremes of LC phase behaviour and the R18 system was selected to explore an intermediate case between them. As shown earlier, addition of a small number of Xe atoms ($\approx 0.6\%$ of the total number of particles) does not significantly change the phase behaviour of the bulk LC.¹⁵ The results of Sec. 5.1 show that also the phase sequence of the confined LC is left unchanged as compared to our previous simulations of the pure LC in the cavity with radius $R = 9$.³

The simulation parameters used here are listed in Table 1. In the confined systems the starting configuration consisted of 12 layers of hexagonally close-packed molecules with the director pointing along the cylinder axis. Periodic boundary conditions were applied in the direction of the cylinder axis. The bulk simulations had 6 layers of molecules and periodic boundaries were applied in the three orthogonal directions x , y and z . Randomly selected GB molecules were replaced with Xe atoms. The starting configuration was equilibrated with PT to $T = 1.3 \dots 2.0$ and the results were recorded from the following production run. From the final configurations of the production run a nematic configuration at $T \approx 1.5$ (just above the bulk SmA-N transition temperature) was selected as the starting configuration for the low-temperature simulations. This configuration was subsequently equilibrated to $T = 0.9 \dots 1.6$ after which the production run followed.

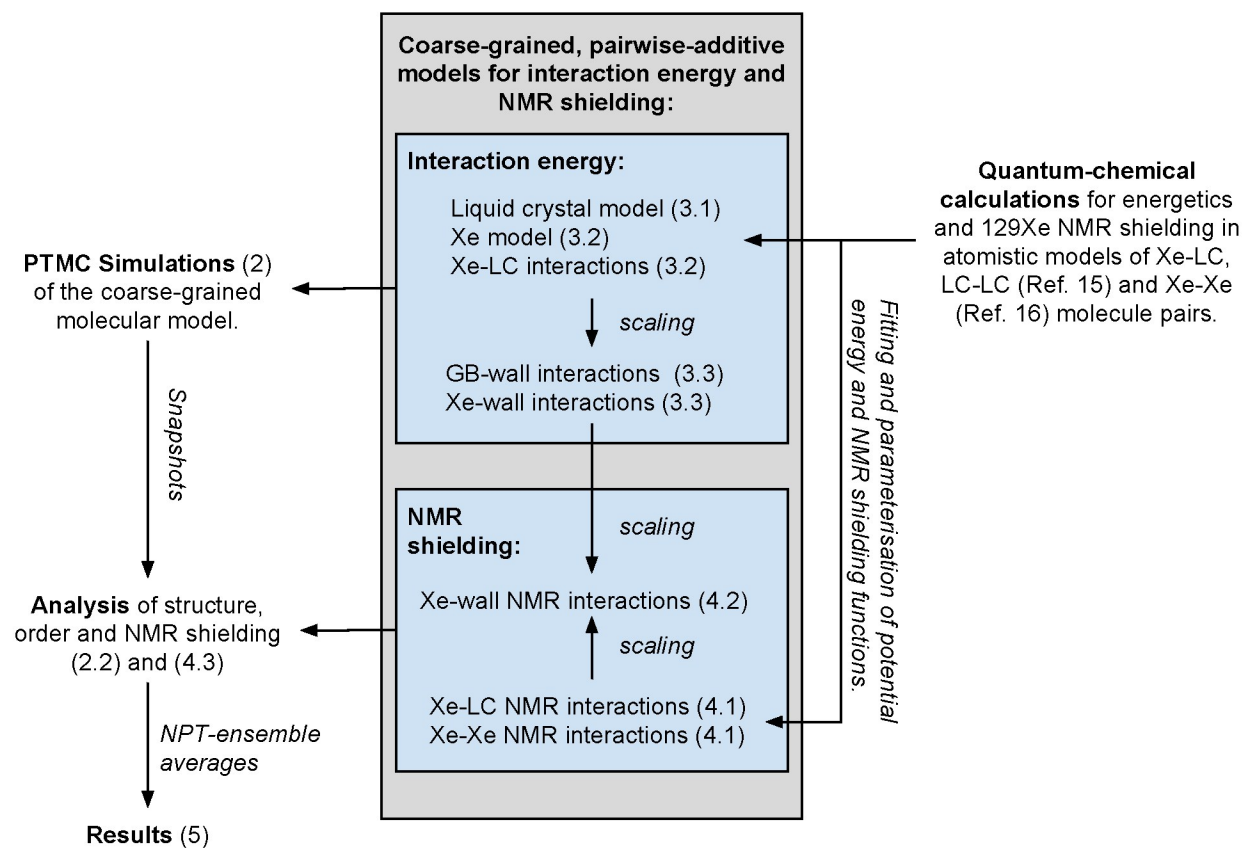


Fig. 1 Flow chart of the methodology used in this paper to calculate nuclear shielding for Xe atoms dissolved in liquid crystal confined to cylindrical cavities. Arrows show the direction of the information flow. The numbers inside parentheses refer to Sections of this paper, where the respective topics are presented.

Table 1 Parameters for the simulations.

	Cylindrical cavity simulations				Bulk	
	R9		R18			
Temperature range ^a	low	high	low	high	low	high
Observed LC phases ^b	Sm	N-PN	Sm	N-PN-I	Cr-Sm	N-I
Number of replicas in parallel tempering	52	46	121	96	52	47
Number of thermalization sweeps $\times 10^5$	3	3	7	3	3	3
Number of production sweeps $\times 10^5$	4	4	4	4	4	4
Directions of volume trials ^c	z	z	z	z	xy, z	xyz
Number of GB (Xe) particles	2576 (16)	2576 (16)	10948 (68)	10948 (68)	1610 (10)	1610 (10)

^a Low: $T = 0.9 \dots 1.6$, high: $T = 1.3 \dots 2.0$.

^b Cr, Sm, N, PN, I and their combinations are listed for the temperature ranges at which the respective phases crystal, smectic(-A), nematic, paranematic and isotropic are observed in the bulk LC and in the cavities.

^c z : the dimension along the long axis of the cavity was changed; xy : the box base area was changed, while the ratio of the box sides L_x/L_y was kept constant; xyz : isotropic volume scaling.

2.1 Monte Carlo update sweeps

The simulation was performed with cyclic update sweeps. One MC sweep consists of trial translations of the Xe atoms, combined trial rotations/translations of all the GB particles and one or more trial volume moves. At every 10th sweep, N_{repl}^3 (N_{repl} is the number of replicas) temperature exchanges between two randomly selected replicas were attempted using the parallel tempering acceptance criterion.^{19,22} At least 3×10^5 MC sweeps of equilibration preceded the production phase in the low temperature simulations and the production run was 4×10^5 sweeps long. The detailed numbers of equilibration and production sweeps for each system are presented in Table 1.

2.2 Analysis of the simulation snapshots

All the results were collected by recording simulation snapshots of each PT replica at every 400th MC sweep after the equilibration run. They were first subjected to appropriate averaging over the particles within the snapshot and, after that, processed with the weighted histogram analysis method for parallel tempering (PTWHAM), to make optimal use of the data from all the replicas.²³ Where present, the error bars in the plots represent two times the standard deviation given by PTWHAM.

3 Molecular model

3.1 Liquid crystal model

The pairwise-additive interactions between the LC molecules are described by the familiar GB potential. The potential is briefly reviewed in Sec. 2 of the ESI.[†] We use the GB potential parametrisation $(\kappa, \kappa', \mu, \nu) = (4.4, 20, 1, 1)$, which has been shown to yield the bulk phase structure Cr – SmA – N – I at the reduced temperature range $T = 0.8 \dots 2.0$, with a fixed reduced pressure $P = 2.0$.^{3,15,20,21} The potential energy curves for the different configurations of a GB dimer with this parametrisation are presented in Fig. 2 b). The range parameter in the GB potential has been approximated to be $\zeta_0 = 4.5 \text{ \AA}$.²⁰ The well-depth parameter, which corresponds to the binding energy in the cross-configuration (Fig. 2) of a GB dimer, was chosen by us to be $\epsilon_0 = 68.11 \text{ meV}$. This is roughly 2.3 times smaller than the quantum-chemically estimated value of Ref. 15 and three times larger than the estimate presented in Ref. 20. The choice of ϵ_0 does not affect the phase structure of the liquid crystal, since it leaves the GB-GB and GB-wall interactions invariant. The value was chosen on empirical grounds, because it enhances the attraction between Xe atoms and GB molecules and was found to reduce accumulation of Xe atoms between smectic layers as discussed in Sec. 3 of the ESI.[†]

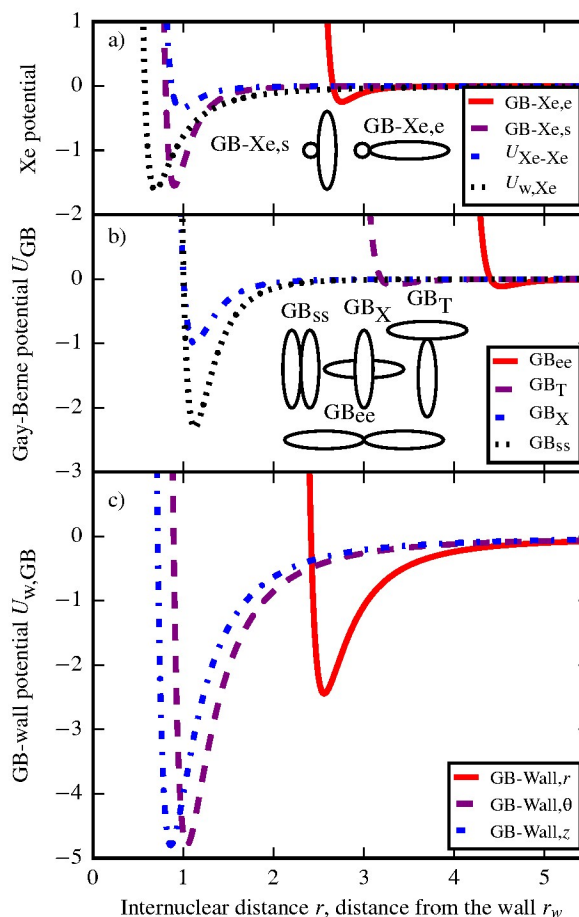


Fig. 2 Potential energy curves for the interactions of GB molecules, Xe atoms and a cylindrical cavity with radius $R = 9$. For the intermolecular interactions, the horizontal axis shows the internuclear distance. For interactions with the wall it represents the distance of the particle centre from the wall. a) GB-Xe,e and GB-Xe,s denote the potential energy curves $U_{\text{GB-Xe}}$ when Xe is at the end and on the side of the GB molecule, respectively. $U_{\text{w,Xe}}$ is for the potential energy between the Xe atom and the cavity wall. $U_{\text{Xe-Xe}}$ is the mutual interaction of two Xe atoms. The insets represent the relative orientations of the GB molecule and the Xe atom in the "side" and "end" configurations. b) GB_T, GB_{ee}, GB_{ss} and GB_X denote the potential energies for the GB-GB interaction in T, end-to-end, side-by-side and cross configurations, respectively. The insets represent the relative orientations of the GB molecules in each case. c) Interactions of a GB particle with the wall. GB-Wall,_r, GB-Wall,_θ and GB-Wall,_z represent potential energies $U_{\text{w,GB}}$ for a GB particle oriented in three orthogonal directions, radial, azimuthal and along the cavity axis, respectively.

We work in the reduced units by scaling all distances with the GB potential range parameter ζ_0 , and all energies with the binding energy of the cross-configuration of a GB dimer, ϵ_0 , and setting $\epsilon_0 = \zeta_0 = 1$. This gives us the following substitutions for reduced pressure P , temperature T and number density $\rho = N/V$:

$$\begin{aligned} P\zeta_0^3/\epsilon_0 &\rightarrow P \\ k_B T/\epsilon_0 &\rightarrow T \\ N\zeta_0^3/V &\rightarrow \rho \end{aligned}$$

From here on, all formulas and quantities are defined in these reduced units, unless explicitly stated otherwise.

3.2 Xe-LC and Xe-Xe interactions

The Xe atoms are described as Lennard-Jones particles. The form of the potential used for the LJ solute - GB solvent interactions is the same as conveyed in Refs. 24 and 25 and employed in Ref. 15. We review it in Sec. 3 of the ESI.[†] The parameters for the GB-Xe potential have been calculated quantum-chemically¹⁵ and are summarised in Table 2. $\epsilon_0^{\text{GB-Xe}} = 1.55$ represents the QC computed value, relative to the present choice of ϵ_0 mentioned earlier. The effects of changing $\epsilon_0^{\text{GB-Xe}}$ are investigated in Sec. 3 of the ESI.[†]

For the Xe-Xe interaction the LJ(12-6) potential was used with the well depth and range parameter $\epsilon_0^{\text{Xe-Xe}} = 0.358$ and $\zeta_0^{\text{Xe-Xe}} = 0.869$, respectively.²⁶ Fig. 2 a) presents the potential energy curves for the "side" and "end" configurations of the GB-Xe pair, as well as the potential energy curve for the Xe dimer within the current parameterisation.

3.3 Interaction between the particles and the cavity wall

The cylindrical cavity is considered to be infinitely long and its wall infinitely thick. The starting point of defining the interaction of the wall and the confined particles was to consider the wall to consist of smoothly and evenly distributed LJ particles. The LC molecule interacts with the wall via two LJ sites embedded to the GB particle²⁷ as shown in the schematic Fig. 3. The interaction potential for a LJ particle and the cylindrical wall has been derived by Zhang, Wang and Jiang²⁸ and can be expressed in the GB units as

$$\begin{aligned} U_w(r_w) &= \epsilon_w \zeta_w^3 \rho_w \left[\frac{63\pi}{64} I_{10}(k, R/\zeta_w) - \frac{3\pi}{2} I_4(k, R/\zeta_w) \right] \\ I_m(k, R) &= \frac{2\pi}{(m-1)R^{m-1}(1-k^2)^{m-1}} \times \\ &\quad {}_2F_1 \left[\frac{-(m-1)}{2}, \frac{-(m-3)}{2}; 1; k^2 \right] \\ k &= 1 - \frac{r_w}{R}, \end{aligned} \quad (1)$$

Table 2 Parameters of the molecular interactions.

Parameter	Value	Unit	Value in GB units
GB-GB potential			
ϵ_0	68.11	meV	1
ζ_0 (Ref. 20)	4.5	Å	1
GB-Xe potential (Ref. 15)			
$\epsilon_0^{\text{GB-Xe}}$	105.57	meV	1.55
$\zeta_0^{\text{GB-Xe}}$	3.6	Å	0.8
$\zeta_e^{\text{GB-Xe}}/\zeta_s^{\text{GB-Xe}}$			3.32
$\epsilon_e^{\text{GB-Xe}}/\epsilon_s^{\text{GB-Xe}}$			0.16
$\mu^{\text{GB-Xe}}$			0.35
Xe-Xe potential (Ref. 26)			
$\epsilon_0^{\text{Xe-Xe}}$	24.40	meV	0.358
$\zeta_0^{\text{Xe-Xe}}$	3.91	Å	0.869
GB-wall potential			
ρ_w	0.010974	Å ⁻³	1
ϵ_w	68.11	meV	1
ζ_w	4.5	Å	1
Xe-wall potential			
ϵ_w^{Xe}	91.26	meV	1.34
ζ_w^{Xe}	3.6	Å	0.8

where r_w is the distance from the center of the particle to the wall. R is the radius of the cavity and ρ_w is the number density of the "virtual" LJ particles that the wall consists of. ϵ_w sets the well-depth of the potential and ζ_w defines the size of the constituent virtual particles in the wall. ${}_2F_1$ is the hypergeometric function as defined in Eq. 15.1.1 of Ref. 29.

For the GB-wall interaction we set $\epsilon_w = \zeta_w = \rho_w = 1$ in Eq. 1. This corresponds to the $K_w = 8.0$ potential strength parameter we have used previously, $K_w = 8\epsilon_w\rho_w\zeta_w^3$.³ The full GB-wall potential is the sum of the interactions of the form (1), corresponding to the two embedded LJ sites.

Fig. 2 c) represents the potential energy curves of the GB-wall interaction for three orientations of the GB molecule. The symmetric placement of the interaction sites at the ends of the GB particle favours homogeneous planar anchoring, the alignment of the molecules along the wall. When the long axis of the LC molecule is parallel to the axis of the cavity, the well-depth of the potential is roughly twice as large as the well-depth of the GB-GB interaction in a side-by-side configuration.

For the Xe-wall interaction we also used a potential of the form of Eq. 1 with the parameters $\zeta_w^{\text{Xe}} = \zeta_0^{\text{GB-Xe}} = 0.8$ and $\epsilon_w^{\text{Xe}} = 1.33989$. In the previously used parameterisation scheme³ we get $K_w^{\text{Xe}} = 5.48819$. The choice of parameters is

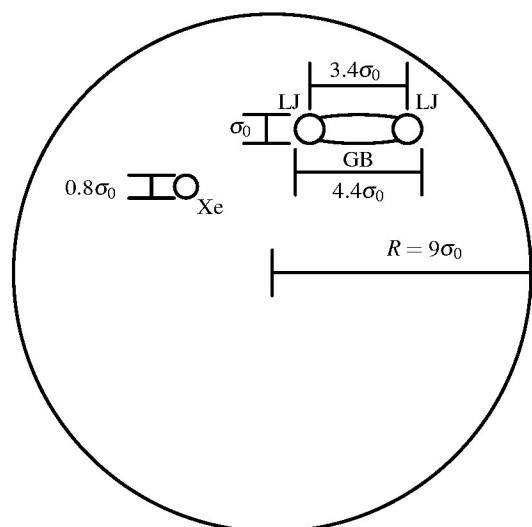


Fig. 3 Schematic representation of the dimensions of a cylindrical cavity with radius $R = 9\sigma_0$, a Gay-Berne particle (GB), embedded Lennard-Jones sites (LJ) and a xenon atom (Xe).

justified in Sec. 5 of the ESI.[†]

4 ^{129}Xe nuclear shielding

We compute the ^{129}Xe nuclear shielding from simulation snapshots in a pairwise-additive manner.¹⁵ The pairwise GB-Xe, Xe-Xe, and Xe-wall interaction contributions to the shielding tensor are defined in suitable local coordinate frames and subsequently transformed to a common axis system before averaging, as explained in Sec. 4.3. The Xe shielding tensor is in this paper considered relative to the shielding of a free Xe atom, $\sigma = \sigma_{\text{full}} - \sigma_{\text{free}}\mathbf{1}$. Here, σ_{free} is the isotropic shielding constant of free Xe atom, $\mathbf{1}$ is the 3×3 unit matrix and σ_{full} is the total shielding tensor.

Molecular simulations give information about the microscopic order and structure of the LC. Calculations of ^{129}Xe parameters from simulations provide a link between the microscopic phenomena and the features of experimental Xe NMR spectra in LCs. In the present case the simulation model gives us insight on the phase behaviour of LCs confined to the voids of mesoporous materials.^{10,11} The largest contribution to the ^{129}Xe nuclear shielding comes from the interactions with the liquid crystal molecules. Xe-Xe interactions occur very rarely and, thus, their contribution to the total shielding is negligible. The wall brings an additional contribution to the ^{129}Xe NMR shielding in the confined systems but, as shown in Sec. 4.2, it is rather short-ranged. Hence, the direct contribution of the

confinement is important only for Xe atoms residing near the cavity wall.

4.1 Xe-GB and Xe-Xe interaction contributions to the ^{129}Xe NMR shielding

The pairwise-additive contributions of the Xe-LC interactions to the ^{129}Xe nuclear shielding were parameterised quantum-chemically for a system of a model LC molecule and Xe atom. The theory and parameterisation have been presented in detail in the work by Lintuvuori, Straka and Vaara.¹⁵ We briefly outline the method in Sec. 6 of the ESI of this Article.[†] The functions used to calculate the tensor elements can be found in the original work by Lintuvuori *et al.*¹⁵

For the Xe_2 shielding relative to a free ^{129}Xe atom we employed the chemical shift and shielding anisotropy functions of Ref. 17. The tensor representation of the shielding contribution and the local coordinate system used for the parameterisation are also reviewed in Sec. 6 of the ESI of this article.[†]

The present model for the ^{129}Xe shielding has been found to correctly reproduce the trends of the Xe chemical shift in the isotropic and nematic phases as well as the discontinuities at the N-I and SmA-N transitions of a bulk LC.¹⁵ However, the magnitude of the Xe shielding in the nematic phase of the GB LC is small $\langle\sigma_{zz}\rangle \approx -120$ ppm¹⁵ as compared to the experimental shielding values found in the range $-217 \dots -198$ ppm, measured in the bulk nematic phase of the Phase IV LC.¹⁰ In the SmA phase, the simulated ^{129}Xe NMR shielding suffered from an excess of Xe atoms squeezed between the smectic layers.¹⁵ In the present work we have suppressed this squeezing phenomenon by increasing the attraction between the Xe atom and the GB molecule, with the result that more Xe atoms are found inside the smectic layers as can be seen from Fig. 2 b) of Sec. 3 in the ESI.[†]

4.2 Xe-wall interaction contributions to ^{129}Xe nuclear shielding

We model the wall as consisting of smoothly and evenly distributed Xe atoms. The contribution of the wall to the ^{129}Xe NMR shielding is formulated by integrating the Xe-Xe shielding tensor components over the wall volume in a pairwise-additive fashion. The process is analogous to the definition of the potential energy between the LJ site and the wall in Sec. 3.3, with some special considerations since we are handling a tensorial quantity here. The coordinate system used to define the final ^{129}Xe -wall shielding tensor is shown in Fig. 5 of the ESI.[†] The Cartesian set of axes is such that the x -axis points from the Xe atom to the radial direction and the z -axis is parallel to the cylinder axis. The cylindrically symmetric Xe-Xe shielding tensor can be represented in arbitrary coordi-

nates as

$$\sigma_{\alpha\beta}^{\text{Xe-Xe}}(r') = \sigma(r')\delta_{\alpha\beta} + \frac{2}{3}\Delta\sigma(r')s_{\alpha\beta}, \quad (2)$$

where $\sigma(r')$ is the isotropic shielding, $\delta_{\alpha\beta}$ is the Kronecker delta, $\Delta\sigma(r')$ is the shielding anisotropy with respect to the internuclear axis and $s_{\alpha\beta}$ is the orientation tensor of the internuclear axis r' :

$$s_{\alpha\beta} = \frac{1}{2}(3\hat{r}'_{\alpha}\hat{r}'_{\beta} - \delta_{\alpha\beta}). \quad (3)$$

The nuclear site symmetry of the system consisting of a single Xe atom and the cylindrical cavity is C_{2v} (except for the rare case that the atom is exactly at the center of the cavity, when the symmetry is $C_{\infty v}$). This implies that the ^{129}Xe -wall nuclear shielding tensor can be represented using only the three independent diagonal components ($\sigma_{xx}^{\text{wall}}$, $\sigma_{yy}^{\text{wall}}$, $\sigma_{zz}^{\text{wall}}$).

These are obtained by integration over the entire wall as

$$\sigma_{\alpha\alpha}^{\text{wall}} = \rho_w \int_{\text{wall}} \left[\sigma(r') + \frac{2}{3}\Delta\sigma(r')s_{\alpha\alpha} \right] dV, \quad (4)$$

where r' is now the vector from the Xe atom to an infinitesimal wall element. For the purpose of simplifying the integration, the quantum-chemically computed isotropic ^{129}Xe NMR shielding $\sigma(r')$ and shielding anisotropy $\Delta\sigma(r')$ of a Xe dimer¹⁷ were fitted to general inverse power series $\sigma(r') = \sum_n \sigma_n/r'^n$, $\Delta\sigma(r') = \sum_n \Delta\sigma_n/r'^n$. Then the series were scaled term-wise with using the strength and range parameters (ϵ_w^{Xe} , ζ_w^{Xe}) and ($\epsilon_0^{\text{Xe-Xe}}$, $\zeta_0^{\text{Xe-Xe}}$) of the Xe-wall and Xe-Xe interaction potentials, respectively. The fit coefficients σ_n , $\Delta\sigma_n$, the scaling and the integration process are presented in Table 1, Sec. 7.1 and Sec. 7.2, of the ESI[†], respectively. In result, we obtain

$$\begin{aligned} \sigma_{xx}^{\text{wall}}(k, R) &= \rho_w \frac{\epsilon_w^{\text{Xe}}}{\epsilon_0^{\text{Xe-Xe}}} \sum_n \left(\frac{\zeta_w^{\text{Xe}}}{\zeta_0^{\text{Xe-Xe}}} \right)^n P_n(k, R) \left[\left(\sigma_n - \frac{\Delta\sigma_n}{3} \right) \tilde{I}_{n-3}^{(0)}(k) + \frac{n-1}{n} \Delta\sigma_n \tilde{I}_{n-3}^{(2)}(k) \right] \\ \sigma_{yy}^{\text{wall}}(k, R) &= \rho_w \frac{\epsilon_w^{\text{Xe}}}{\epsilon_0^{\text{Xe-Xe}}} \sum_n \left(\frac{\zeta_w^{\text{Xe}}}{\zeta_0^{\text{Xe-Xe}}} \right)^n P_n(k, R) \left[\left(\sigma_n - \frac{\Delta\sigma_n}{3} + \frac{n-1}{n} \Delta\sigma_n \right) \tilde{I}_{n-3}^{(0)}(k) - \frac{n-1}{n} \Delta\sigma_n \tilde{I}_{n-3}^{(2)}(k) \right] \\ \sigma_{zz}^{\text{wall}}(k, R) &= \rho_w \frac{\epsilon_w^{\text{Xe}}}{\epsilon_0^{\text{Xe-Xe}}} \sum_n \left(\frac{\zeta_w^{\text{Xe}}}{\zeta_0^{\text{Xe-Xe}}} \right)^n P_n(k, R) \left(\sigma_n - \frac{\Delta\sigma_n}{3} + \frac{1}{n} \Delta\sigma_n \right) \tilde{I}_{n-3}^{(0)}(k). \\ P_n(k, R) &= \frac{2\sqrt{\pi}\Gamma[\frac{1}{2}(n-1)]}{\Gamma[\frac{n}{2}](n-3)R^{n-3}(1-k^2)^{n-3}}, \end{aligned} \quad (5)$$

where R is the inner radius of the cavity and $k = 1 - r_w/R$, r_w being the distance from the particle centre to the wall. To fit the shielding in the ^{129}Xe dimer to $\sigma(r')$ and $\Delta\sigma(r')$, we used terms with odd n , since they were easier to implement robustly in to the analysis program. We chose to use $n = 11, 13, \dots, 35$ and did not find any practical improvement by including the terms with even n . The expansions for the coefficients $P_n(k, R)$ and the integrals $\tilde{I}_{n-3}^{(m')}(k)$, both resulting from the integration over the angular coordinate, can be found in Sec. 7.2 of the ESI.[†]

The resulting ^{129}Xe -wall shielding tensor components are presented in Fig. 4 a). Although the plots for σ_{yy} and σ_{zz} look very similar, they are not identical, as can be seen from the inset of Fig. 4 a) and Eq. 5. σ_{yy} approaches σ_{zz} as the cavity gets larger and the curvature of the wall becomes less significant. At the limit $R \rightarrow \infty$ the components become identical and for very large cavities it would be sensible to use a slab wall model. The magnitude of σ_{xx} , the radial component, is

significantly smaller than that of the two other components.

This model for the Xe-wall interactions is a very rough one but since the NMR interactions are typically rather short-ranged, it can be expected that the contribution of the wall to the ^{129}Xe shielding will be small if the Xe atoms do not stay close to the wall during most of the simulation time. In Sec. 5.3 we will see that the direct contributions of the wall to the Xe shielding are small regardless of temperature.

4.3 Averaging the ^{129}Xe nuclear shielding tensor components

Each pair-interaction contribution to the ^{129}Xe shielding tensor was transformed to a common coordinate system for averaging. For the confined R9 and R18 systems, the Xe shielding tensor was averaged in the coordinate frame of the simulation box, where the z -axis coincides with the axis of the cylindrical cavity. For the bulk system the z -axis was defined by the in-

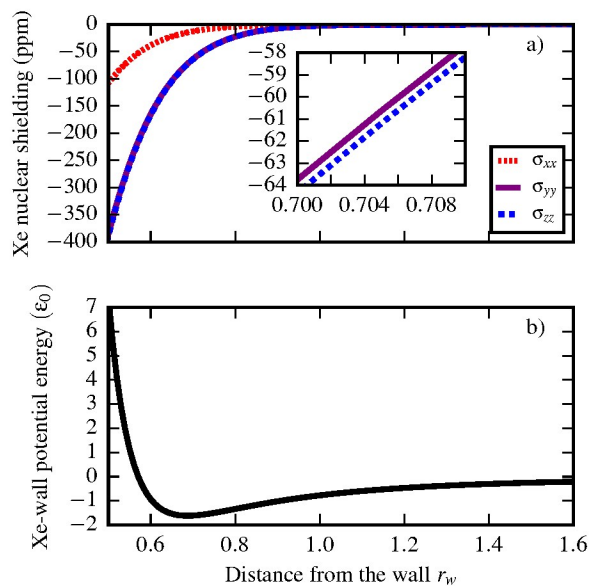


Fig. 4 a) Components of the nuclear magnetic shielding tensor of the ^{129}Xe nucleus as a result of Xe-wall interaction in the cavity with radius $R = 9$. The corresponding analytical expressions are presented in Eq. 5. The three orthogonal axes are chosen so that the x -axis points in the radial direction and the z -axis points to the direction of the cylinder axis. The inset illustrates the small difference between the yy and zz components. Note the different scale in the inset. b) The corresponding Xe potential energy curve due to interaction with the wall.

stantaneous LC director in each simulation snapshot. The two other axes were defined by the two other eigenvectors of the orientational ordering tensor. In practice the choice between the two coordinate systems does not change the results for the confined LCs, since the director remains practically always parallel to the cavity axis.

For each snapshot, the observable component of the ^{129}Xe nuclear shielding along the z -axis ($\langle\sigma_{zz}\rangle$), the isotropic shielding ($\langle\sigma^{\text{iso}}\rangle = \frac{1}{3}\langle\sigma_{xx} + \sigma_{yy} + \sigma_{zz}\rangle$) and the component of the anisotropic shielding along the z -axis ($\langle\sigma_{zz}^{\text{aniso}}\rangle = \frac{2}{3}\langle\Delta\sigma\rangle = \frac{2}{3}\langle\sigma_{zz} - \frac{1}{2}(\sigma_{xx} + \sigma_{yy})\rangle$) were computed by averaging over all Xe atoms. Ensemble averages of the ^{129}Xe NMR shielding components were calculated by reweighting the results of all simulation snapshots with PTWHAM.²³ The observable Xe nuclear shielding results from a sum of isotropic and anisotropic contributions through

$$\begin{aligned} \langle\sigma_{zz}\rangle &= \langle\sigma^{\text{iso}}\rangle + \langle\sigma_{zz}^{\text{aniso}}\rangle = \langle\sigma^{\text{iso}}\rangle + \frac{2}{3}f(\theta) \sum_{\alpha,\beta} \langle s_{\alpha\beta}^{\hat{d}} \sigma_{\alpha\beta} \rangle \\ &\approx \langle\sigma^{\text{iso}}\rangle + \frac{2}{3} \sum_{\alpha,\beta} S_{\alpha\beta}^{\hat{d}} \langle\sigma_{\alpha\beta}\rangle, \end{aligned} \quad (6)$$

where $s_{\alpha\beta}^{\hat{d}}$ is the orientation tensor of the LC director, and $S_{\alpha\beta}^{\hat{d}}$ is its average. θ is the angle between the external magnetic field and the LC director. $f(\theta) = \frac{3}{2}\cos^2\theta - \frac{1}{2}$ is the second degree Legendre polynomial in $\cos\theta$. We set the magnetic field along the cavity axis in the confined systems. In the simulations, the director is nearly all the time parallel to the cavity axis, $f(\theta = 0) = 1$. The second line of Eq. 6 holds exactly if the orientation tensor and the local shielding tensor $\sigma_{\alpha\beta}$ can be considered uncorrelated. We use the full form of the first line of Eq. 6 to calculate the observable ^{129}Xe nuclear shielding σ_{zz} .

5 Simulation results and discussion

5.1 Order parameters

The orientational order parameter P_2 and translational order parameter τ_1 , computed with respect to the LC director, are commonly used to detect the uniaxial nematic and smectic- A phases, respectively. The definitions of these parameters are given in Sec. 4 of the ESI.[†] $P_2 = 1$ indicates that all molecules are perfectly aligned along a common axis. Correspondingly, $\tau_1 = 1$ indicates that the molecules are perfectly arranged in layers perpendicular to the director. Order parameter value zero refers to perfect orientational or translational disorder/randomness for P_2 or τ_1 , respectively. In Fig. 5 we show P_2 and τ_1 as functions of temperature for the two confined systems R9 and R18, as well as for the bulk system.

In a previous study we simulated cylindrically confined pure LCs in cavities with radii $R = 7, 9$ and 11 .³ It was found that the director of the LC was strongly aligned with the cavity axis. Moreover, the cavity wall sustained the nematic order at temperatures above the bulk N-I transition temperature ($T_{\text{NI}} = 1.64$). Going to higher temperatures, the orientational order decreased smoothly from the nematic to the paranematic phase, and only well above T_{NI} did the LC become isotropic at the center of the cavity, with radius $R = 9$. A genuinely isotropic phase was not observed at all for temperatures $T < 2.0$. From Fig. 5 a) we see that all these findings about the orientational order of the pure GB LC in the cavity with radius $R = 9$, apply also here to the R9 system with the dissolved Xe atoms.

Interestingly, the R18 system is already large enough to exhibit an almost bulk-like isotropic phase above $T = 1.9$, where it already has a very low orientational order parameter, $P_2 < 0.125$. However, since the orientational order is higher as compared to the bulk LC, this phase could also be labelled as paranematic. The transition between the nematic and isotropic phases in the R18 system is still a smooth one, as compared to the bulk N-I transition. This transition is also slightly shifted to a higher temperature but to a lesser extent than in the narrower R9 system. The broadened

and shifted transition region of the R18 system, in the range $1.7 < T^* < 1.9$, can best be described as a paranematic phase. Due to the continuously changing nature of the orientational order in the confined systems, the exact temperature of the N-PN transition is not easily defined.

Kityk et al.⁷ noted that the smooth wall raises the nematic – paranematic transition temperature T_{NPN} . In real systems factors such as wall irregularities decrease the ordering imposed by the confinement. Thus, the location of the N-PN transition – above or below bulk T_{NI} – depends on the morphology of the pores.

In an earlier NVT ensemble simulation in a cavity of radius $R = 20$, with wall consisting of fixed atoms, the nematic director was seen to settle perpendicular to the axis of the cavity.³⁰ The reason for this could be the chosen condition of constant volume or the form of the particle-wall interaction in that work. In the present work, the director is all the time nearly parallel to the cavity axis for both R9 and R18 systems. As seen already in Ref. 3, sampling the NPT ensemble better reproduces the phase changes in both the bulk and the cavities, an observation confirmed by the present results. This indicates also a better microscopic description and, hence, the presently observed parallel alignment appears more realistic.

The formation of smectic layers in the confined LC is similar to the bulk case. The wall acts as a weak inhibitor of the layering of the molecules.³ This is seen in Fig. 5 b), in the SmA phase around $T = 1.35$, where the translational order parameter of the R9 system, $\tau_1 = 0.55$, is distinctly smaller than the one for the bulk system, $\tau_1 = 0.67$. The SmA-N transition for the R18 system occurs exactly at the same temperature as in the bulk, as shown in Fig. 5 b).

5.2 Orientation parameter profiles

Figs. 6 a) and f) show how the orientational order parameter with respect to the cylinder axis behaves as a function of distance from the cavity wall at different temperatures and LC phases. The values were calculated by dividing the cavity to cylindrical shells of width $b = 0.1$ and averaging over the LC molecules with midpoints located in each shell.

From our previous work³ we know that the cavity wall strongly enhances orientational order, but at high temperatures ($T > 1.9$), in cavities large enough ($R = 11$), the core region of the cavity is isotropic. At temperatures below $T = 1.3$, the presence of a smooth wall initiates a wave-like density modulation which partially prevents the appearance of crystalline order emerging from the self-organisation of the LC.³

From Fig. 5 a) we observe that the R9 system is in the PN phase while the R18 system is almost isotropic at $T = 1.97$, the highest temperature profiled in Fig. 6. From the P_2 profiles of Figs. 6 a) and f) we see that the orientational order decays towards the center in both cavities but the inner re-

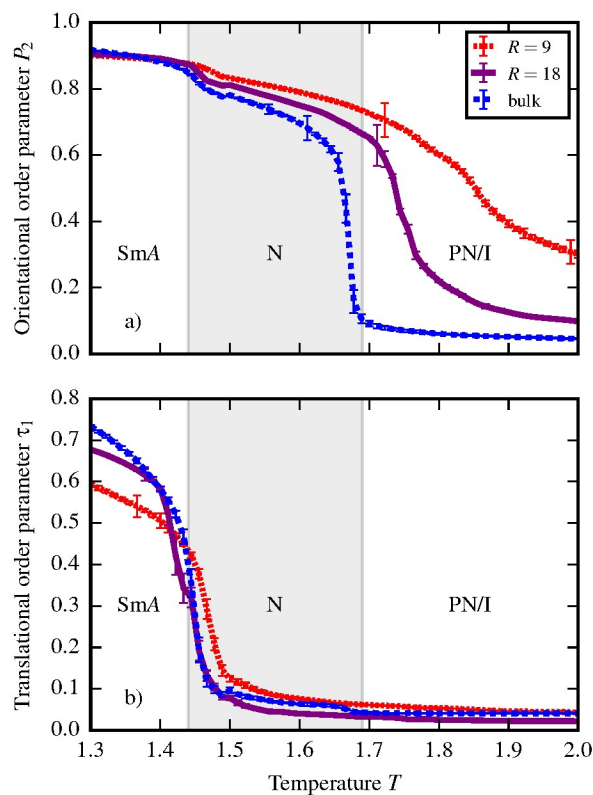


Fig. 5 a) Orientational order parameter P_2 and b) translational order parameter τ_1 as a function of temperature in the two confined systems with radii $R = 9$ and $R = 18$, as well as in the bulk. The background shading in this and the following figures refers to the phases obtained in the simulation of the bulk system.

gion with small P_2 is larger in the R18 system, resulting in the different overall P_2 of the two systems. At the slightly lower temperature, $T = 1.74$, the R18 system exhibits PN behaviour as the orientational order decays steadily towards the centre of the cavity, reaching a low value of $P_2 < 0.2$, while the LC of the R9 system possesses already a high orientational order, $P_2 > 0.57$ throughout the cavity. In the latter case, the LC is clearly nematic. At lower temperatures, $T = 1.52$ and $T = 1.30$, the orientational order is only slightly higher close to the wall than elsewhere in the cavity. In all the orientational order parameter profiles there are similar small local extrema, which convert to steps in the curves for the isotropic and paranematic phases, where the orientational order decreases steeply away from the wall. The extrema are due to layering of the GB molecules on the wall as indicated by the aforementioned density waves in Fig. 3 b) of the ESI†.

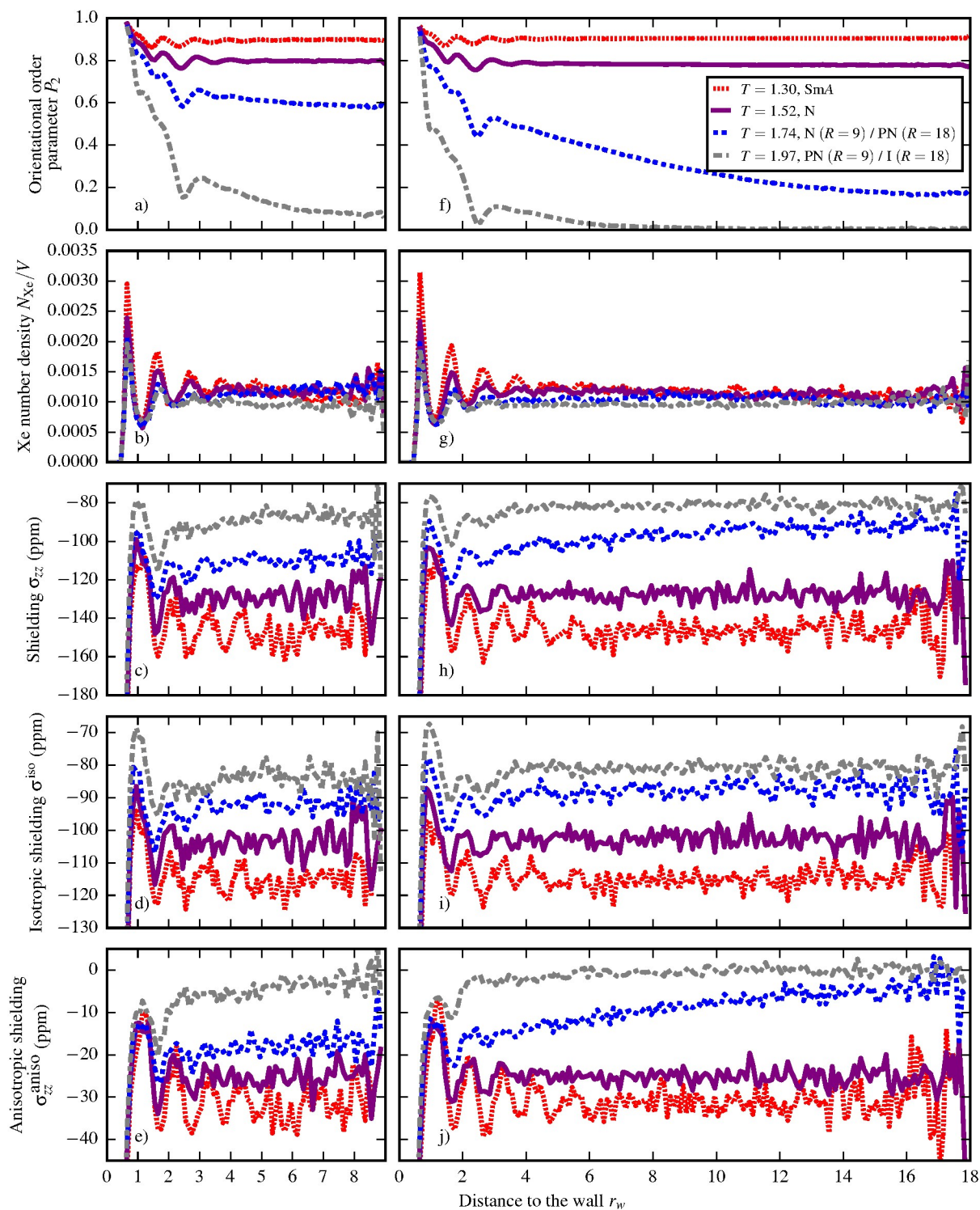


Fig. 6 Average NMR shielding (ppm) of atomic ^{129}Xe dissolved in a model liquid crystal confined to cylindrical nanocavities. Results as a function of distance to the wall in the two cavities with radii $R = 9$ (left) and $R = 18$ (right) at four different temperatures and LC phases. Panels a) and f) present the respective profiles for the orientational order parameter P_2 . Profiles of the number density of the Xe atoms N_{Xe}/V are presented in panels b) and g). Panels c)-e) and h)-j) present the observable ^{129}Xe NMR shielding (ppm) along the cavity axis σ_{zz} , the isotropic shielding σ^{iso} and the anisotropic shielding with respect to the cavity axis $\sigma_{zz}^{\text{aniso}}$.

5.3 ^{129}Xe NMR shielding

The ^{129}Xe NMR shielding parameters computed from the present simulations as a function of temperature for the three different systems R9, R18 and the bulk LC, are compared in Fig. 7. The plots show how the phase transitions and structural changes in the coarse-grained uniaxial thermotropic LC are reflected by our quantum-chemically parameterised pairwise-additive Xe nuclear shielding model.

Features seen in the orientational order parameter curves in Fig. 5 a) – the sharp N-I transition in the bulk and the smooth N-PN transition in the small cavity with radius $R = 9$ – are mirrored in the behaviour of the anisotropic ^{129}Xe nuclear shielding $\langle\sigma_{zz}^{\text{aniso}}\rangle$ in Fig. 7 c). The anisotropic contribution is included in the observable shielding $\langle\sigma_{zz}\rangle$ through Eq. 6. The NMR parameters for the larger cavity with radius $R = 18$ stay expectedly in between the curves for the bulk LC and the R9 system. Looking at $\langle\sigma^{\text{iso}}\rangle$ in Fig. 7 b), we observe that the isotropic ^{129}Xe nuclear shielding in the pore with radius $R = 18$ is shifted to the negative direction from the bulk case by roughly as much as $\langle\sigma^{\text{iso}}\rangle$ in the cavity with $R = 9$ is shifted with respect to the larger ($R = 18$) cavity. The simulated ^{129}Xe nuclear shielding $\langle\sigma_{zz}\rangle$ for the smallest system R9 grows quite linearly with the temperature, but in the larger R18 system the steeper paranematic transition can be seen as a change of slope in the curve of Fig. 7 a) and also (albeit less clearly) in the isotropic shielding in Fig. 7 b).

The signature of the SmA-N transition, a change of slope in the dependence of $\langle\sigma_{zz}\rangle$ and $\langle\sigma_{zz}^{\text{aniso}}\rangle$ on temperature, is absent from the NMR parameters of the confined systems. As before,¹⁵ it reveals itself in the bulk system, however: there is a change of slope in $\langle\sigma_{zz}\rangle$ and particularly $\langle\sigma_{zz}^{\text{aniso}}\rangle$ at $T \approx 1.45$. This missing feature in the ^{129}Xe NMR shielding curves of the confined systems can be explained by looking at the distribution of the Xe atoms in the cavity and the distribution of translational order, in Fig. 6 of the ESI.[†] (The calculation of the translational order profile is discussed in Sec. 8 of the ESI.[†]) From our previous study, we know that the translational order is suppressed near the cavity wall.³ In the cylindrical geometry, a large fraction of the volume of the cavity is close to the cavity wall and so is a large portion of the Xe atoms. These considerations are confirmed by the present simulations. Hence, the Xe atoms sample largely a region where there is no strong smectic order, but where other factors, such as the wall-induced density wave, shape the local LC phase.³ Experimentally the change of slope at the SmA-N transition has been attributed at least partly to Xe atoms slightly preferring the interlayer space of the SmA phase.³¹ In our bulk simulations, a slight preference of the interlayer space also occurs, but in the confined LC this redistribution of Xe atoms is virtually non-existent. This is also one of the causes why the SmA-N transition is not observed in the simulated ^{129}Xe

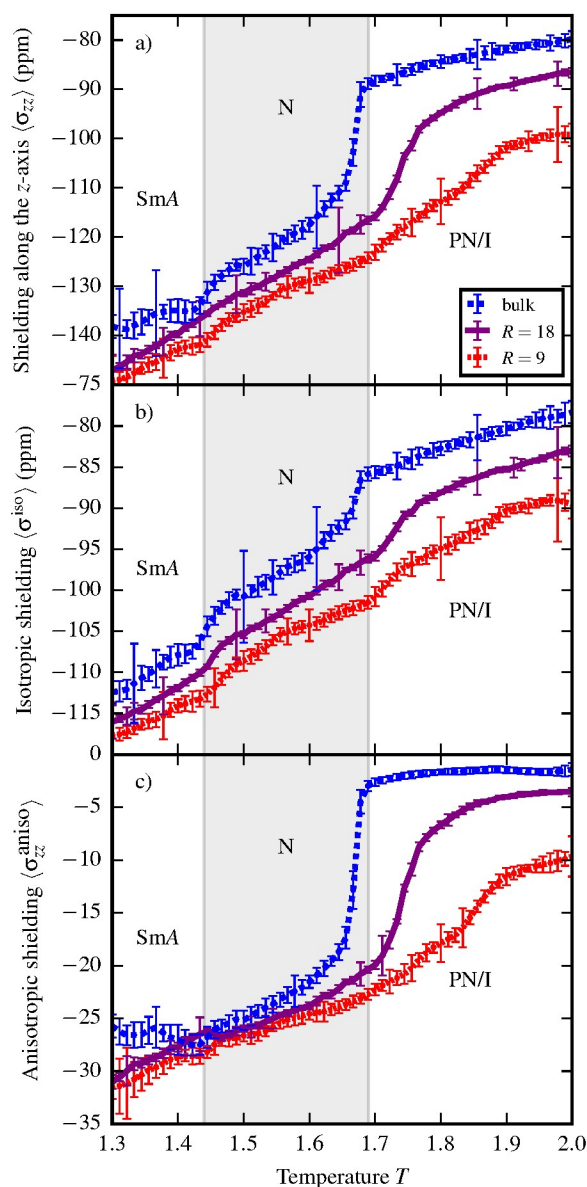


Fig. 7 Comparison of the ^{129}Xe NMR shielding (as referenced to free Xe atom) of dissolved atomic Xe in a model liquid crystal in two cylindrical cavities with radii $R = 9$ and $R = 18$, as well as in bulk LC. a) The observable component of the ^{129}Xe nuclear shielding along the cavity axis (σ_{zz}) is composed of b) the isotropic shielding (σ^{iso}) and c) the component of the anisotropic shielding along the cavity axis ($\sigma_{zz}^{\text{aniso}}$), as in $\sigma_{zz} = \sigma^{\text{iso}} + \sigma_{zz}^{\text{aniso}}$. The background shading refers to the phases obtained in the simulation of the bulk system.

NMR shielding curves.

The experimentally observed NMR shielding for ^{129}Xe dis-

solved in a nematic Phase IV LC confined to a controlled pore glass (CPG) with pore diameter 156 Å lies around -201 ppm.¹⁰ With the unit of length $\zeta_0 = 4.5$ Å,¹⁵ our cavity with radius $R = 18$ is of comparable size to the voids in this CPG material. Compared to experiments, our model gives a range of considerably smaller values $\langle\sigma_{zz}\rangle = -136..-117$ ppm, when the LC is nematic. There is an improved agreement with experiment as compared to the results reported in Ref. 15 (for bulk LC) due to the more attractive GB-Xe interaction used presently. A quantitative agreement with experiment cannot realistically be expected with the present, extremely coarse-grained model. However, it is likely that the agreement with experiment could be further improved at the point where the LC molecule is made flexible. Inclusion of the currently neglected relativistic effects in the parameterisation¹⁵ of the ^{129}Xe -LC NMR shielding model would increase the magnitude of the shielding and, hence, bring the results closer to the experiments. In addition, the parameterisation was done with density-functional theory calculations and the quantitative errors involved can be substantial in weakly bound systems.³²⁻³⁴ The pairwise additivity approximation also contributes to a systematic error in the ^{129}Xe nuclear shielding, albeit in Xe_n clusters this error was in the direction of too large interaction effects on Xe shielding.¹⁶

The contributions of the Xe-wall interaction to the ^{129}Xe shielding in the two cavities with radii $R = 9$ and $R = 18$ are presented in Fig. 8. The figure shows that the direct effect of the wall to the Xe shielding (in Fig. 7) is weak as compared to the shielding contribution from the Xe-GB interactions, as anticipated. The Xe atoms interact more with the wall in the smaller cavity, as expected. Thus, all the NMR parameters in the smaller cavity with $R = 9$ are shifted to the negative direction as compared to the larger cavity with $R = 18$. In the temperature range $T = 1.3..2.0$, the wall contributions seem to be almost temperature-independent. Distribution of the LC particles with respect to the wall is temperature-dependent and this could in principle affect the distribution of Xe atoms in the cavity and their interactions with the wall. Temperature-dependent Xe-wall shielding could also be observed if the Xe-wall interaction would directly cause a temperature-dependent radial distribution of the Xe atoms and the Xe atoms would e.g. accumulate near the wall at low temperatures. The contribution of the wall interaction to the observable shielding $\langle\sigma_{zz}\rangle$ is between -11.5 (-6) and -9.5 (-4.5) ppm in the R9 (R18) system. From Fig. 8 b) we observe that the Xe-wall interaction is mostly responsible for the offset between the curves of the isotropic shielding, $\langle\sigma^{\text{iso}}\rangle$, between the R9, R18 and bulk cases in Fig. 7 b). Using Eq. 6 and Fig. 8 we can say that roughly 3/4 of the direct Xe-wall interaction contribution to the ^{129}Xe nuclear shielding comes from the isotropic component and the anisotropic component amounts to the remaining quarter in both confined systems R9 and R18.

If the strength of the average interaction between the Xe atoms and the cavity wall were trivially related to the surface-to-volume ratio of a cylindrical cavity, the ^{129}Xe NMR shielding would be proportional to the inverse of the diameter of the cavity, as $(2R)^{-1}$. At least for small cavities the case is not that simple, though, since the wall-induced order of the LC does not have a simple dependence on cavity size as discussed below in Sec. 5.4. On the other hand, for cavities considerably larger than R18, the direct shielding effect is expected to be rather small due to a smaller surface-to-volume ratio.

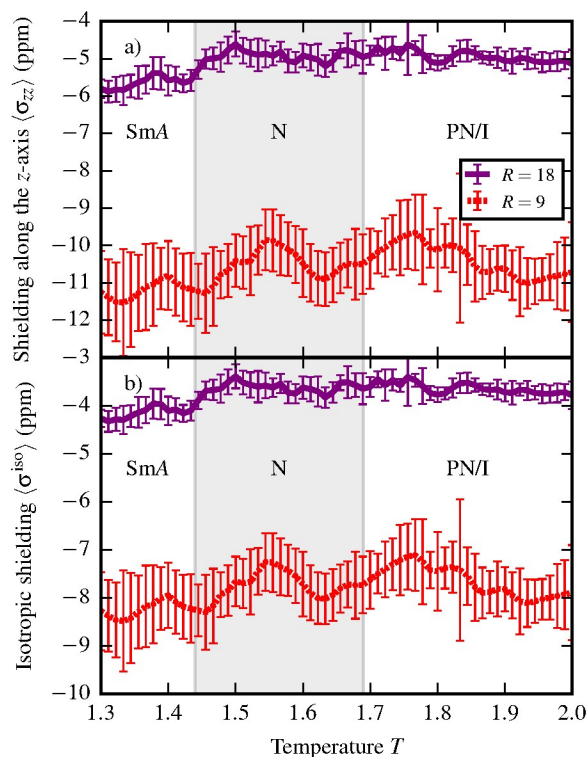


Fig. 8 Comparison of the wall contribution to the ^{129}Xe NMR shielding (referenced to free Xe atom) of dissolved atomic Xe in a model liquid crystal in two cylindrical cavities with radii $R = 9$ and $R = 18$. a) The observable component of the ^{129}Xe nuclear shielding along the cavity axis $\langle\sigma_{zz}\rangle$ is related to b) the isotropic shielding $\langle\sigma^{\text{iso}}\rangle$ and the anisotropic shielding with respect to the cavity axis $\langle\sigma_{zz}^{\text{aniso}}\rangle$ through $\sigma_{zz} = \sigma^{\text{iso}} + \sigma_{zz}^{\text{aniso}}$. The background shading refers to the phases obtained in the simulation of the bulk system.

A bulk LC, such as Phase IV, with positive anisotropy of diamagnetic susceptibility, orients itself along the external magnetic field in NMR experiments. Thus, the observed ^{129}Xe chemical shift (with respect to a low-pressure Xe gas) is equal to $-\sigma_{zz}$. In contrast, in the case of LC confined to CPG materials with small pore size, it is assumed that the LC di-

rector is parallel to the axis in each cylindrical pore.¹⁰ With an isotropic orientational distribution of the pore axes with respect to the magnetic field, the mean ^{129}Xe chemical shift observed from the pores equals the negative of the isotropic component in Eq. 6. The anisotropic component still affects the line shape of the spectra. Fig. 7 concerns the isotropic and anisotropic Xe nuclear shielding, the latter as referenced to the direction of the cavity axis. This would correspond to experiments with aligned pores and enables comparison of bulk and confined systems and isotropic to anisotropic contribution in both.

Fig. 9 represents the more common experimental situation, where Xe chemical shift, instead of shielding, is observed in isotropically distributed pore directions. The figure shows the simulated isotropic ^{129}Xe chemical shifts in the R9 and R18 systems and the chemical shift along the field for the bulk system. The corresponding experimentally recorded ^{129}Xe chemical shifts from the pores of CPG81 and CPG156, as well as in bulk LC are shown in Fig. 7 of Ref. 10. The qualitative resemblance of the simulated and experimental chemical shifts is significant: The N-I transition was hardly experimentally observed in CPG81 and CPG156 and the observable chemical shift was nearly linear from 199 ppm to 188 ppm, in the temperature range where the corresponding bulk LC transformed from the solid to the isotropic phase, via a nematic intermediate phase.¹⁰ In the bulk phase, the N-I transition was clearly seen. All these features are reproduced by our simulated ^{129}Xe chemical shifts in Fig. 9.

Additional features where simulations reproduce the experimental results¹⁰ for the ^{129}Xe chemical shift include the small nonlinearity of slope as a function of temperature just below the bulk N-I transition temperature in CPG156, and just above the transition temperature in the R18 system. Fig. 5 shows that this nonlinearity coincides with the paranematic phase. In CPG156 this feature occurs below the bulk transition, most likely due to the disorder arising from the pore interconnects and the roughness of the inner surface of the pores. These factors are absent from the single, smooth cylindrical pore of the simulations. In general, the surface morphology of the pores may have a considerable effect on the observed ^{129}Xe chemical shift.

At the temperatures where the bulk LC is isotropic, the simulated chemical shifts in Fig. 9 behave linearly, similarly to the experiments.¹⁰ In both cases, the wall contributions shift the curves for the confined systems above the ^{129}Xe chemical shift in bulk LC. In the experimentally recorded chemical shifts, the difference between the chemical shifts in CPG81 (CPG156) and in bulk LC are only ≈ 2 ppm (< 1 ppm). The chemical shift difference in the corresponding simulated systems R9 (R18) and bulk LC is about 9 ppm (4 ppm) at the highest temperature $T = 2.0$. From Fig. 8 b) we see that roughly 8 ppm (4 ppm) of this difference can be explained by

the direct interaction of the Xe atoms with the wall. Hence it seems that in our model, the contribution of the Xe-wall interaction to the ^{129}Xe nuclear shielding is overestimated. This is partly due to our choice of $\epsilon_0 = 68.11$ meV, which is significantly smaller than the quantum-chemically obtained value $\epsilon_0 = 157.58$ meV. This choice indirectly scales up (by about the factor of 2.3) the Xe-wall shielding (Eq. 5) via the ϵ_w^{Xe} parameter, as in Eq. 12 of the ESI.[†]

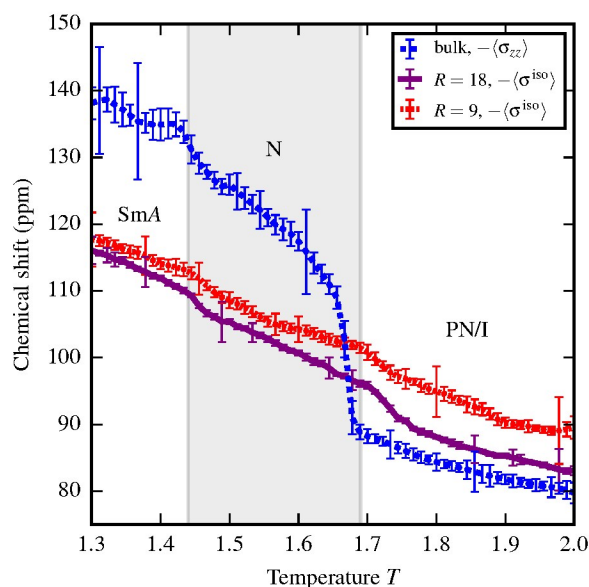


Fig. 9 The simulated isotropic ^{129}Xe chemical shift, $-\langle\sigma^{\text{iso}}\rangle$ for Xe dissolved in LC confined to cylindrical cavities with two different radii (with the cavity axes isotropically distributed with respect to the magnetic field) as well as the simulated chemical shift along the direction of the magnetic field, $-\langle\sigma_{zz}\rangle$ for Xe dissolved in a bulk LC. The background shading refers to the phases obtained in the simulation of the bulk system.

5.4 ^{129}Xe nuclear shielding profiles

It is interesting to see how the variations of density and orientation parameter in different parts of the cavity (Fig. 6) are reflected in the nuclear shielding experienced by a dissolved ^{129}Xe atom. In Fig. 6 we present the profiles of the average zz -component of the ^{129}Xe NMR shielding tensor, $\langle\sigma_{zz}\rangle$, the isotropic shielding, $\langle\sigma^{\text{iso}}\rangle$, and the anisotropic shielding, $\langle\sigma_{zz}^{\text{aniso}}\rangle$. As with the orientational order parameter profiles, the cavity was divided to cylindrical shells of thickness $b = 0.1$. The nuclear shielding was averaged over Xe atoms with midpoints in each shell. To give an idea of the relative weight of each shell in the total ^{129}Xe NMR shielding, we also include in Fig. 6 b) and g) the profiles of the average number density of Xe atoms, $\langle N_{\text{Xe}}/V \rangle$, as a function of the distance from the

wall of the cavity. Since we keep the thickness of the shell constant, the volume of the shell at distance $R - r_w$ from the centre of the cavity is $2\pi(R - r_w)bL_z$, where L_z is the length of the cylinder. So, the volume of a shell decreases linearly with respect to distance from the wall. The combined effect of the density variations of the Xe atoms and the dependence of the shell volume on r_w on the number of Xe atoms in one shell is shown in Fig. 6 b) and d) of the ESI.[†]

The Xe shielding profiles can be roughly divided to two regions: 1) Where $r_w < 0.65$ the Xe-wall contribution dominates the ^{129}Xe nuclear shielding profiles in Figs. 6 c)-e) and h)-j). This is seen by a comparison to the Xe-wall shielding tensor components in Fig. 4 a). The magnitude of the wall contribution to the Xe shielding rises steeply when the distance to the wall r_w decreases. However, as the distance to the wall gets shorter, the density profiles of the Xe atoms in Figs. 6 b) and g) decrease steeply and on average less than 7% (4%) of the Xe atoms occupy the region $r_w < 0.7$ in the R9 (R18) system. The result is that the direct contribution of the wall to the system-wide average ^{129}Xe nuclear shielding is relatively small as was seen earlier in Fig. 8. 2) Away from the wall, where $r_w > 0.7$, the dominant factor in the ^{129}Xe shielding is the contribution of the LC molecules. In the region $1 < r_w < 3$, the ^{129}Xe NMR shielding profiles reflect the density variations of the Xe atoms in Fig. 6 b) and g). Since the Xe atoms are very few, the density variation of the Xe particles has its roots in the density wave of the GB particles, which was seen earlier in Fig. 3 b) of the ESI[†], as well as in our previous work.³

In the system with radius $R = 18$, at $T = 1.74$, we can see a signature of the PN behaviour as the anisotropic ^{129}Xe nuclear shielding in Fig. 6 j) decays towards zero when approaching the cavity centre, corresponding to the similar behaviour of the orientational order parameter (in the panel f) of the same figure). The center region of the cavity tends to be isotropic, provided that the cavity is large enough. The difference in $\sigma_{zz}^{\text{aniso}}$ between the centre of the cavity ($r_w = 18$) and near the wall ($r_w = 1$) is roughly 15 ppm. This difference is translated to σ_{zz} according to Eq. 6. In the smaller cavity, with radius $R = 9$, the same connection between the local anisotropic ^{129}Xe NMR shielding and the local orientational order is seen at the higher temperature, $T = 1.97$ in Fig. 6 e).

6 Conclusion

We have simulated the NMR shielding of ^{129}Xe dissolved in uniaxial Gay-Berne model liquid crystal confined to smooth-walled cylindrical nanocavities. The constant-pressure parallel tempering Monte Carlo method was used to cover a temperature range where smectic-A, nematic, paranematic and isotropic phases were observed. Two cavities with different radii, $R = 9$ and $R = 18$, were studied, as well as a bulk

LC. A quantum-chemically preparametrised pairwise-additive model was used to compute the average ^{129}Xe nuclear shielding tensors and the local shielding felt by the Xe atom in different parts of the cavity.

In accord with the earlier study of some of the present authors on pure LCs confined in cavities,³ the LC-wall interaction favoured planar anchoring and the director was found to point along the axis of the cavity in the oriented phases of the confined systems. In the larger cavity with radius $R = 18$, we found at the highest simulated temperatures an almost isotropic phase that changes smoothly to a nematic phase via a paranematic phase, when going to lower temperature. The smooth change of orientational order is reflected in the anisotropic ^{129}Xe NMR shielding where the transition is clearly observed. For the smaller cavity with radius $R = 9$ we did not observe the isotropic phase. The gentle, gradual transition from paranematic to nematic phase, upon decreasing temperature, is less obvious in the ^{129}Xe NMR shielding. The smoothness of the transition in small cavities can also make it hard to observe it experimentally. Our simulation model with cavity radius $R = 18$ reproduced the nonlinear dependence of the isotropic ^{129}Xe nuclear shielding on the temperature near the bulk N-I transition, observed in the experimental chemical shift for Xe dissolved in LC confined to controlled pore glass material CPG156. Comparison with the simulated orientational order parameters reveals that this nonlinearity appears when a smooth transition between nematic and isotropic phases via a paranematic phase takes place.

The SmA-N transition was not seen in the ^{129}Xe NMR shielding curves of the confined systems. This non-feature was attributed to the effect of Xe atoms sampling largely the volume close to the wall where the layering of LC molecules is suppressed. In the bulk system the SmA-N transition appears as a change of slope in the anisotropic contribution to the ^{129}Xe nuclear shielding and, consequently, in the shielding tensor component parallel to the LC director, $\langle\sigma_{zz}\rangle$.

The ^{129}Xe NMR shielding parameters become increasingly more negative with respect to bulk LC phase as a function of decreasing cavity diameter. The reason for this is the additional cavity wall contribution, that is small for a large cavity and becomes relatively more important in smaller cavities due to the increasing surface-volume ratio. A qualitative agreement was found between the isotropic ^{129}Xe NMR shielding simulated here and the earlier, experimentally recorded chemical shift of ^{129}Xe dissolved in LC confined to controlled pore glasses with corresponding pore radii. The contribution of the Xe-wall interaction to the Xe chemical shift could be brought closer to experimental values by a refined parameterisation scheme.

The detailed relation of the cavity size to the magnitude of the ^{129}Xe nuclear shielding is somewhat complex in small cavities, due to the interplay of the wall-induced orientational

order and the self-organisation of the LC: The decay of orientational order away from the wall is steeper for the large cavity as compared to the small one. It also occurs at a lower temperature than in the smaller cavity. This is the source of the different kind of paranematic behaviour in the average order occurring in the two systems and is also seen in the simulated profiles of the anisotropic ^{129}Xe nuclear shielding and in the component of the shielding along the cavity axis, $\langle\sigma_{zz}\rangle$.

While we have kept our simulation model rather general and simple, we can still differentiate between the many details found in confined LC systems and resolve effects that merge into the experimentally observed Xe NMR spectra. With the kind of simulations presented in this work, it is possible to analyse Xe NMR experiments in porous materials with realistic pore dimensions. Our model makes it feasible to investigate even larger cavities and the orientational order resulting from the combined effect of the confinement and the anisotropic magnetic susceptibility of the medium.

7 Acknowledgements

J.K. would like to thank the Finnish Cultural Foundation for funding this research. Further support was received from Academy of Finland grants 125316 (P.L.), 250813 (J.V.) and 258565 (J.V.), Tauno Tönnig foundation (J.V.), and University of Oulu (J.V.). M.S. was supported by Czech Science Foundation, grant 14-03564S. The project was additionally supported by the Research Council of University of Oulu (M.S. and J.V.) CSC - IT Center for Science and the Finnish Grid Initiative project provided the computational resources.

References

- G. P. Crawford and S. Žumer, *Liquid Crystals in Complex Geometries; Formed by Polymer and Porous Networks*, Taylor & Francis, London, 1996.
- P.-G. de Gennes and J. Prost, *The Physics of Liquid Crystals*, Clarendon Press, Oxford, 2nd edn, 1993.
- J. Karjalainen, J. Lintuvuori, V.-V. Telkki, P. Lantto and J. Vaara, *Phys. Chem. Chem. Phys.*, 2013, **15**, 14047–14057.
- S. Calus, B. Jablonska, M. Busch, D. Rau, P. Huber and A. V. Kityk, *Phys. Rev. E*, 2014, **89**, 062501.
- S. Calus, D. Rau, P. Huber and A. V. Kityk, *Phys. Rev. E*, 2012, **86**, 021701.
- A. V. Kityk and P. Huber, *Appl. Phys. Lett.*, 2010, **97**, 153124.
- A. V. Kityk, M. Wolff, K. Knorr, D. Morineau, R. Lefort and P. Huber, *Phys. Rev. Lett.*, 2008, **101**, 187801.
- J. Jokisaari, *Prog. Nucl. Magn. Reson. Spectrosc.*, 1994, **26**, 1–26.
- J. Lounila, O. Muenster, J. Jokisaari and P. Diehl, *J. Chem. Phys.*, 1992, **97**, 8977–8985.
- P. Tallavaara, V.-V. Telkki and J. Jokisaari, *J. Phys. Chem. B*, 2006, **110**, 21603–21612.
- P. Tallavaara and J. Jokisaari, *Phys. Chem. Chem. Phys.*, 2006, **8**, 4902–4907.
- V.-V. Telkki, J. Lounila and J. Jokisaari, *J. Phys. Chem. B*, 2005, **109**, 24343–24351.
- H. W. Long, M. Luzar, H. C. Gaede, R. G. Larsen, J. Kritzenberger, A. Pines and G. P. Crawford, *J. Phys. Chem.*, 1995, **99**, 11989–11993.
- J. P. Jokisaari, A. M. Kantola, J. A. Lounila and L. P. Ingman, *Phys. Rev. Lett.*, 2011, **106**, 017801.
- J. Lintuvuori, M. Straka and J. Vaara, *Phys. Rev. E*, 2007, **75**, 031707.
- M. Hanni, P. Lantto and J. Vaara, *Phys. Chem. Chem. Phys.*, 2009, **11**, 2485–2496.
- M. Hanni, P. Lantto, M. Iliaš, H. J. Aa. Jensen and J. Vaara, *J. Chem. Phys.*, 2007, **127**, 164313.
- J. G. Gay and B. J. Berne, *J. Chem. Phys.*, 1981, **74**, 3316–3319.
- T. Okabe, M. Kawata, Y. Okamoto and M. Mikami, *Chem. Phys. Lett.*, 2001, **335**, 435–439.
- M. A. Bates and G. R. Luckhurst, *J. Chem. Phys.*, 1999, **110**, 7087–7108.
- E. de Miguel, E. del Rio and F. Blas, *J. Chem. Phys.*, 2004, **121**, 11183–11194.
- J. D. Chodera and M. R. Shirts, *J. Chem. Phys.*, 2011, **135**, 194110.
- J. D. Chodera, W. C. Swope, J. W. Pitera, C. Seok and K. A. Dill, *J. Chem. Theory Comput.*, 2007, **3**, 26–41.
- D. J. Cleaver, C. M. Care, M. P. Allen and M. P. Neal, *Phys. Rev. E*, 1996, **54**, 559–567.
- H. Fukunaga, J. Takimoto and M. Doi, *J. Chem. Phys.*, 2004, **120**, 7792–7800.
- M. Hanni, P. Lantto and J. Vaara, *Phys. Chem. Chem. Phys.*, 2011, **13**, 13704–13708.
- D. Micheletti, L. Muccioli, R. Berardi, M. Ricci and C. Zannoni, *J. Chem. Phys.*, 2005, **123**, 224705.
- X. Zhang, W. Wang and G. Jiang, *Fluid Phase Equilib.*, 2004, **218**, 239–246.
- M. Abramowitz and I. A. Stegun, *Handbook of Mathematical Functions with Formulas, Graphs, and Mathematical Tables*, Dover Publications, 10th edn, 1972.
- Q. Ji, R. Lefort, R. Busselez and D. Morineau, *J. Chem. Phys.*, 2009, **130**, 234501.
- B. Jagadeesh, A. Prabhakar, M. H. V. Ramana Rao, C. V. S. Murty, V. G. K. M. Pisipati, A. C. Kunwar and C. R. Bowers, *J. Phys. Chem. B*, 2004, **108**, 11272–11279.
- M. Straka, P. Lantto and J. Vaara, *J. Phys. Chem. A*, 2008, **112**, 2658–2668.
- S. Standara, P. Kulhánek, R. Marek and M. Straka, *J. Comput. Chem.*, 2013, **34**, 1890–1898.
- S. Standara, P. Kulhánek, R. Marek, J. Horníček, P. Bouř and M. Straka, *Theor. Chem. Acc.*, 2011, **129**, 677–684.